Eur. Phys. J. B **17**, 57–68 (2000)

THE EUROPEAN PHYSICAL JOURNAL B

EDP Sciences

Mechanical detection of nuclear spin relaxation in a micron-size crystal

O. Klein[1,a], V.V. Naletov[2], and H. Alloul[1,b]

[1] Laboratoire des Solides Irradiés, École Polytechnique, 91128 Palaiseau, France
[2] Physics Department, Kazan State University, Kazan, 420008, Russia

Received 23 February 2000

Abstract. A room temperature nuclear magnetic resonance force microscope (MRFM), fitted in a 1 tesla electromagnet, has been used to measure the nuclear spin relaxation of ^{1}H in a micron-size (70 ng) crystal of ammonium sulfate. NMR sequences, combining both pulsed and continuous wave radio-frequency fields, have allowed us to measure mechanically T_2 and T_1, the transverse and longitudinal spin relaxation times. Because two spin species with different T_1 values are measured in our 7 μm thick crystal, magnetic resonance imaging of their spatial distribution inside the sample section have been performed. To understand quantitatively the measured signal, we carefully study the influence of spin-lattice relaxation and non-adiabaticity of the continuous-wave sequence on the intensity and time dependence of the detected signal.

PACS. 07.79.Pk Magnetic force microscopes – 76.60.-k Nuclear magnetic resonance and relaxation – 87.61.Ff Instrumentation

1 Introduction

For a long time research groups have looked for new ways of detecting electronic or nuclear paramagnetic resonance with better sensitivity. A review of different proposed methods can be found in the introduction of Abragam's book [1]. In two seminal papers [2,3], Sidles recognized the advantage of coupling the spin system to a mechanical oscillator for magnetic resonance imaging. In this technique, the force signal is proportional to the magnetic field gradient [4], which, in an extremely inhomogeneous field, should allow high spatial resolution. The new technique is referred to as magnetic resonance force microscopy (MRFM) [5].

The first magnetic resonance force signal was detected by Rugar *et al.* in 1992 while exciting electron spin resonance (eMRFM) in a 30 ng crystal of diphenylpicrylhydrazil [6]. Two years later, Rugar *et al.* reported the mechanical detection of ^{1}H (protons) nuclear magnetic resonance (nMRFM) in 12 ng of ammonium nitrate [7]. These two pioneering experiments demonstrate that a microfabricated cantilever, identical to the ones developed for atomic force microscopy, can detect the magnetic moment of a micron-size sample. In the case of nuclear magnetic resonance (NMR) [7], the achieved sensitivity of 10^{13} spin, at room temperature and in a field of 2.4 T, represents a substantial improvement over the standard coil detection.

Significant progress has been made in the past few years. In 1996, Zhang *et al.* mechanically detected the ferromagnetic resonance (fMRFM) of yttrium iron garnet [8]. Imaging experiments with eMRFM [9,10], nMRFM [11,12] and fMRFM [13] were performed. A magnetic resonance torque signal in a homogeneous magnetic field [14] was also detected. Improvement of the force sensitivity by operating at low temperatures [15–17] was demonstrated. Force maps of the sample were obtained with the magnetic probe placed on the mechanical resonator in eMRFM [18] and fMFRM [13]. The highest sensitivity reported so far is around 200 electron spin in a 1 Hz bandwidth. The result was obtained by operating an eMRFM at 77 K in a very large magnetic field gradient [19]. In 1996, Wago *et al.* demonstrated that a pulse sequence combined with fast adiabatic passages can allow measurement of the nuclear spin-lattice relaxation time of ^{19}F in calcium fluoride at low temperatures [15]. The same method was used to measure the longitudinal spin relaxation of ^{1}H in ammonium sulfate at room temperature and normal pressure [20,21]. Recent eMRFM work in vitreous silica at 5 K showed that the same principles can be also applied to study electron spin dynamics of E' centers with long T_1 [17].

In this paper, we report the first measurements of both the transverse and longitudinal nuclear spin dynamics of ^{1}H using mechanical detection. A very thin sample

[a] *Present address:* Service de Physique de l'État Condensé, CEA Orme des Merisiers, 91191 Gif-Sur-Yvette, France
e-mail: `oklein@cea.fr`
[b] *Present address:* Laboratoire de Physique des Solides, Université Paris-Sud, 91405 Orsay Cedex, France

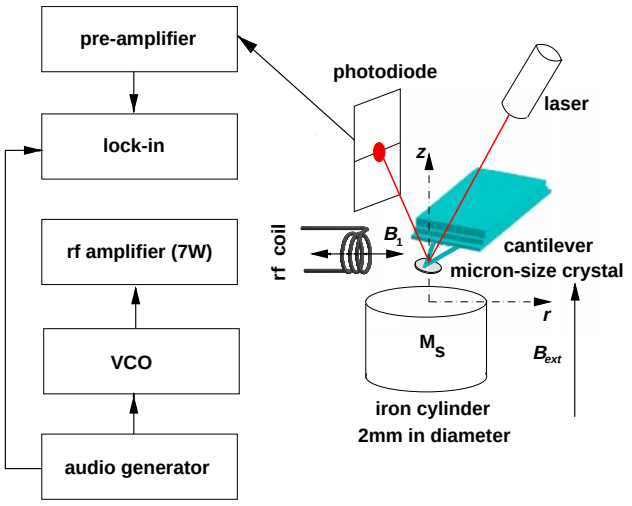

Fig. 1. MRFMs are miniature versions of the Faraday balance. The instrument fits between the poles of an electromagnet that generates a homogeneous static field $B_{\rm ext} = 1$ T. A sample is affixed onto a micro-fabricated cantilever and placed in a field gradient $g \approx 500$ T/m produced by a 2 millimeter-size iron bar. The gradient serves to create a magnetic force on the spin system. The induced Å-scale bending of the cantilever is measured by a laser beam deflection on a photodiode. To increase the sensitivity, the nuclear magnetization is inverted periodically at 1.4 kHz, a frequency that corresponds to the fundamental flexure mode of the cantilever. The induced vibration is monitored by a lock-in. The nuclear spin oscillations are obtained by cyclic adiabatic inversions using a frequency modulated r.f. field produced by a VCO. The carrier is at the Larmor frequency of protons.

is used to analyze if new phenomena might be specific to small sizes. Our instrument is a simple home-built MRFM located inside a 1 tesla electromagnet. The mechanical motion of the cantilever is monitored by a laser beam deflection system. The sample is a 7 μm thick crystal of $(NH_4)_2SO_4$. Two spin-lattice relaxation times are observed, $T_{1s} = 0.4$ s and $T_{1l} = 5$ s. The latter value corresponds to the T_1 reported in the literature for this compound [22,23]. The short relaxation, however, might be due to water contamination inside the crystal during its contact with air. These same two relaxation times are also measured by conventional NMR in powder samples with particles of dimensions smaller than 50 μm.

After introducing in Section 2 the measurement technique employed in this study, we will present in Section 3 our results on the transverse and longitudinal spin relaxation properties of $(NH_4)_2SO_4$. This will be followed in Section 4 by a more detailed analysis of the time dependence and magnitude of the force signal in order to quantify the proportion of spins with short and long T_1 and to determine the effect of the non-adiabaticity of the sequence in the measured signal. Finally a model to describe our experimental data will be proposed.

2 Measurement of the force signal

The setup is schematically represented in Figure 1. The experiment is performed at room temperature inside a vacuum cell (10^{-2} torr) constantly connected to the inlet of a rotary pump. The instrument [24] fits between the poles of an iron core electromagnet which produces a static magnetic field $B_{\rm ext}\mathbf{k}$ along the z axis. To the uniform field one adds a second inhomogeneous field with axial symmetry produced by a magnetized iron bar 8 mm in length and 1.9 mm in diameter. The polarization field experienced by the spin is $B_0 = B_{\rm ext} + B_{\rm cyl}$, with $B_0 = \mathbf{B}_0 \cdot \mathbf{k}$ and $B_{\rm cyl} = \mathbf{B}_{\rm cyl} \cdot \mathbf{k}$. Near the symmetry axis, the instantaneous magnetic force acting on the sample is given by the expression [25]:

$$F(t) = \int_{V_{\rm s}} M_z(\mathbf{r}, t) \frac{\partial B_{\rm cyl}}{\partial z} {\rm d}V. \qquad (1)$$

Here M_z is the z component of the bulk magnetization and $V_{\rm s}$ is the volume of the sample. For small sample size, we make the approximation that the field gradient $g = \partial B_{\rm cyl}/\partial z$ is uniform over $V_{\rm s}$. A new length variable $\zeta = B_0(\mathbf{r})/g$ is defined so that a plane of constant ζ maps onto a surface (actually a paraboloid) of constant polarization field which also corresponds to a sheet where the spins have the same motion. A paraboloid of fixed ζ value, however, shifts axially away from the iron cylinder when $B_{\rm ext}$ increases. In this experiment, the sample is placed 0.70 mm above the iron cylinder and centered on the cylinder axis. At this distance, the calculated axial field gradient is $g = -470$ T/m (see Appendix A).

The mechanical force detection is obtained by measuring the elastic deformation along the z axis of a micro-fabricated cantilever on which the sample is attached. In this orientation, the probe is sensitive to the longitudinal component of the nuclear magnetization in contrast with a standard coil detection. The cantilever equation of motion is represented by a damped harmonic oscillator with a single degree of freedom. The measurement technique uses the optical deflection of a 4 μW HeNe laser beam which reflects off the rear side of the cantilever onto a position-sensitive detector.

Our test compound is $(NH_4)_2SO_4$. This non-magnetic insulator has a high proton density $d = 6.4 \times 10^{22}$ ^{1}H/cm^3 and is in its paraelectric state above 223 K. NMR measurements of the ^{1}H spin-lattice relaxation time at 300 K in our powder [26] give $T_{1z} \approx 5$ s along the static field [27]. The ^{1}H linewidth is 5 G and the second moment is $M_2 = 4$ G^2 at 295 K [28]. Our sample is a crystal cleaved to a platelet aspect ratio and glued with epoxy on the end of a commercial Si_3N_4 amorphous cantilever of spring constant $k = 0.008$ N/m, as can been seen in Figure 2. After completing the assembly, the cantilever resonance frequency drops from 5.8 kHz to 1.4 kHz due to the sample mass [29]. The quality factor of the loaded cantilever is $Q \approx 4\,000$ in vacuum. From the electron microscopy images (Fig. 2), the sample dimensions are approximately $100 \times 50 \times 7$ μm^3 with the smallest length (the thickness) oriented along the axial field. This represents a volume

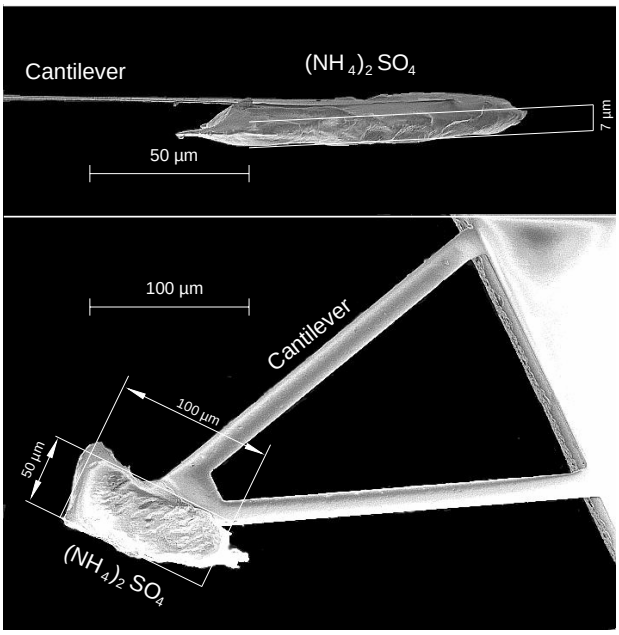

Fig. 2. Images of a commercial Si_3N_4(amorphous) cantilever: a 7 μm thick single-crystal $(NH_4)_2SO_4$ sample is glued on the cantilever end with epoxy. The loaded cantilever has a resonance frequency of 1.4 kHz, a spring constant of 0.008 N/m and a quality factor of 4 000 in vacuum. The estimated sample volume is 3.5×10^{-8} cm^3.

$V_\mathrm{s} = 3.5 \times 10^{-8}$ cm^3 or a mass $m = 70$ ng and corresponds to $N \approx 10^{15}$ protons. The temperature of the cantilever holder is stabilized around +27 °C during the measurement [30]. The nuclear magnetization at thermal equilibrium is expressed by the Curie law $\mathbf{M}_0 = (d\mu_\mathrm{n}^2 B_0/k_\mathrm{B}T)\,\mathbf{k}$, with $\mu_\mathrm{n} = 1.4 \times 10^{-26}$ J/T the proton magnetic moment, $T = 300$ K and $B_0 = 1.3$ T the polarization field. This gives a magnetic moment $M_0 V_\mathrm{s} = 2.3 \times 10^{-16}$ J/T.

In order to increase the sensitivity, M_z is modulated at a frequency ω_m close to ω_c, the frequency of the fundamental flexure mode of the cantilever. At the moment, the optimal configuration uses cantilevers that have mechanical resonance frequencies in the audio range and Larmor frequencies ω_0 which are several orders of magnitude larger (radio or microwave frequencies). Only two methods have been used to create an oscillatory force on the cantilever: cyclic saturation and cyclic adiabatic inversion. They are restricted respectively to compounds that have spin-lattice relaxation times T_1 either shorter or larger than the oscillation period of the cantilever.

In our case, the modulation of $\mathbf{M}$ is generated by a continuous-wave (c.w.) sequence that consists of periodic adiabatic fast passages [1]. The radio-frequency (r.f.) source is a 35-75 MHz Voltage Controlled Oscillator (VCO). The r.f. output field is amplified up to 7 W and fed into an impedance matched resonating circuit ($Q_\mathrm{rf} \simeq 100$) tuned to a fixed frequency, 54.7 MHz. A small coil (3 turns, 0.8 mm in diameter) is in series with the tank circuit. The sample is 0.5 mm away from this antenna. The nuclear spins are irradiated for a few seconds by a linearly polarized r.f. field $B_x = 2B_1 \cos \int_0^t \omega(t')\mathrm{d}t'$ with $\omega(t) = \Omega \sin(\omega_\mathrm{m} t) + \omega_0$, a sine-wave modulation of the r.f. frequency around the proton Larmor frequency $\omega_0 = \gamma\, g\, \zeta_0$, where $\gamma/2\pi = 4.258$ kHz/G is the nuclear gyromagnetic ratio. The surface of constant $\zeta = \zeta_0$ is called the resonant sheet. The sinusoidal frequency modulation is started at a time $t = 0$. In a transformation to a rotating coordinate system with an instantaneous angular velocity $\omega(t)\mathbf{k}$, the effective magnetic field is:

$$\mathbf{B}_\mathrm{e}(\zeta, t) = B_1 \mathbf{i} + \left\{ g\,\zeta - \frac{\omega(t)}{\gamma} \right\} \mathbf{k}. \tag{2}$$

θ is defined as the polar angle made by the apparent field with the external field. The magnetization, however, precesses about the direction $\mathbf{B}_\mathrm{e} + \dot{\theta}/\gamma\,\mathbf{j}$, with $\dot{\theta} = \partial\theta/\partial t$ (see Appendix B). A parameter for non-adiabaticity is defined with $\tan\alpha = \dot{\theta}/(\gamma|\mathbf{B}_\mathrm{e}|)$ the angle between the two vectors. Provided that the adiabatic condition $\alpha \ll 1$ is satisfied, the spin system remains at all times in a state of internal equilibrium and $\mathbf{M}$ is parallel to $\mathbf{B}_\mathrm{e}$ as required by Curie's law. The longitudinal magnetization is $M_z(\zeta, t) = |\mathbf{M}| \cos\theta$, where

$$\cos\theta = \frac{g\,\zeta - \omega(t)/\gamma}{\sqrt{\{g\,\zeta - \omega(t)/\gamma\}^2 + B_1^2}}\,. \tag{3}$$

For free spins, $|\mathbf{M}|$ is a constant of the motion [1]. This is no longer true in condensed matter because of spin-lattice relaxation. In our sample, however, the magnetization decay is slow compared to the modulation period. Under our measurement protocol, an extra defocusing originates from the lack of adiabaticity of the modulation. In a first step, these effects are neglected and they will be considered in a more detailed analysis, deferred to a later section (see also Appendix B). At time $t = 0$, B_1 is assumed to be turned on adiabatically with the sample initially in thermal equilibrium. In this case the norm M reflects the state of the longitudinal magnetization immediately before the force measurement. During the c.w. sequence, the oscillatory movement of $M_z(t)$ comes principally from the $\cos\theta$ factor. The value is expanded in time series $\cos\theta \approx a_0 + a_1 \sin(\omega_\mathrm{m} t)$ [31] with a_1 the first harmonic Fourier component [11] (higher harmonics have a negligible effect on the motion of the cantilever). Because of the large field inhomogeneities, the amplitude of oscillation depends on the location inside the sample. The resonant sheet, which is the paraboloid of constant ζ_0, corresponds to the surface of maximum amplitude of oscillation. The spatial dependence of $a_1(\zeta)$ is the sensitivity profile. Γ is the half width at half maximum of this bell-shaped curve. Γ has the units of a distance and it defines the thickness of the slice probed. The amplitude of Γ depends on both Ω and B_1 [32]. The induced vibration is synchronously amplified by a lock-in technique through a single-pole low-pass linear filter of time constant τ_l. For $\omega_\mathrm{m} = \omega_\mathrm{c}$, the lock-in signal grows exponentially (an exact expression will be given in Eq. (11)) to the asymptotic amplitude

$$A_0 = \frac{1}{\sqrt{2}} \frac{Q\,g}{k} \int_{V_\mathrm{s}} M_0\, a_1(\zeta)\, \mathrm{d}\zeta. \tag{4}$$

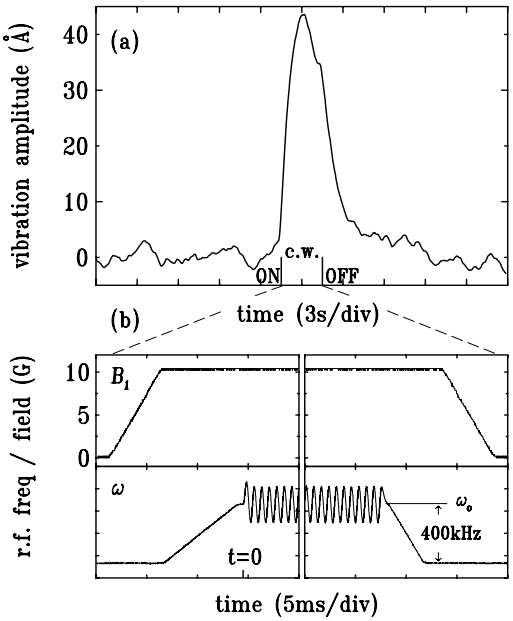

Fig. 3. (a) Vibration amplitude of the cantilever measured by the lock-in for a $(NH_4)_2SO_4$ crystal containing 10^{15} protons at 300 K in $B_{\rm ext} = 0.9425$ T. The trace corresponds to a single shot experiment with no averaging. The lock-in time constant is $\tau_{\rm l} = 0.3$ s. (b) Details of the start and end of the c.w. sequence. The crystal is irradiated for 3 s by a r.f. field of $B_1 = 10$ G (upper panel). The bottom panel shows the voltage waveform applied to the VCO. It produces a sinusoidal frequency modulation around $\omega_0/2\pi = 54.7$ MHz. The amplitude of the modulation is $\Omega/2\pi = 150$ kHz. The width of the curve is the digitalization noise of the oscilloscope (not the phase noise).

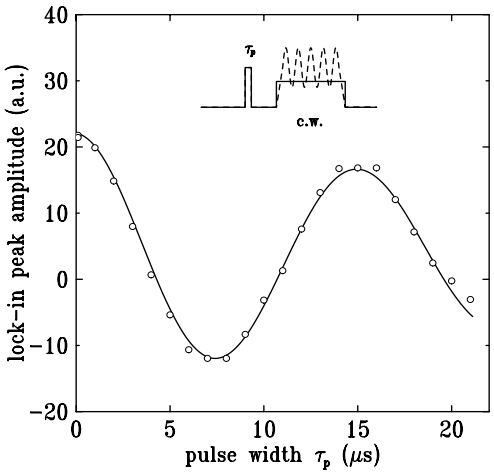

Fig. 4. The amplitude of the force signal (lock-in peak amplitude averaged over 1 s around its maximum) is shown as a function of the width of a r.f. pulse applied 13 ms before the c.w. sequence. Each point is the average of 16 c.w. sequences. The solid line is proportional to a damped $\cos\varphi$ with $\varphi = \gamma\tau_{\rm p}B_1$ the nutation angle. The 6.4 W r.f. power during the pulse corresponds to a rotating field of $B_1 = 15$ G at the sample location. The settings for the c.w. sequence are a r.f. field of 10 G, $\Omega/2\pi = 50$ kHz and $\tau_{\rm l} = 100$ ms. The inset is a schematic of the time dependence of B_1 (solid line) and ω (dashed line).

In conclusion, the lock-in output is proportional to the longitudinal magnetic moment inside the probed slice at the beginning of the c.w. sequence. In the ideal case of a uniform inversion of all spins inside the sample ($a_1 = 1, \forall\zeta$), the asymptotic amplitude would be $A_{\rm tot} = QgM_0V_{\rm s}/(k\sqrt{2})$.

The upper panel of Figure 3 shows the time dependence of the lock-in output $A(t)$. The c.w. sequence is applied between the markers. The time delay between force measurements is set to 27 s ($> 5T_1$) to ensure a steady state magnetization close to the thermal equilibrium value. The lock-in time constant is $\tau_{\rm l} = 0.3$ s which corresponds to an output noise of 4 Å. The bottom panel of Figure 3 displays the time dependence of B_1 and ω at the beginning and end of the c.w. sequence. At the start, the amplitude of B_1 is turned on from 0 to 10 G in 5 ms when the frequency is well off-resonance, *i.e.* 400 kHz below $\omega_0/2\pi$. The frequency is then ramped to resonance in 7 ms. Finally, the frequency modulation of the r.f. field is applied for 3 s with a deviation $\Omega/2\pi = 150$ kHz. For these settings, the calculated value of $\Gamma = 7$ μm is comparable to the sample thickness.

Since the r.f. tank circuit is tuned to a fixed frequency, the resonance is found by sweeping the external field $B_{\rm ext}$. There is *no* spurious vibrations of the cantilever induced by the r.f. fields when $B_{\rm ext}$ is outside the resonance range. Figure 3a shows the amplitude of the lock-in signal achieved in a one shot experiment at the resonance maximum, $B_{\rm ext} = 0.9425$ T. The maximum vibration amplitude is around 40 Å which corresponds to a signal to noise ratio of 20 dB. The shape of the lock-in signal $A(t)$ depends on the value $B_{\rm ext}$ [17]. For $B_{\rm ext} = 0.9425$ T, *i.e.* ζ_0 set at the middle of the sample thickness, *no* steady-state vibrations of the cantilever are induced by the c.w. sequence and the lock-in signal decays toward zero for long a sequence. On the other hand, for $B_{\rm ext} \neq 0.9425$ T, an unbalanced partial repolarization of the magnetization occurs during each cycle and the lock-in signal decays to a finite value which changes sign for $B_{\rm ext}$ smaller or larger than 0.9425 T.

3 Relaxation measurements

In this section the nuclear spin dynamics of our sample are measured by applying a series of r.f. pulses before the c.w. sequence described above.

In order to calibrate the strength of the r.f. field, a r.f. pulse of duration $\tau_{\rm p}$ is applied, with an amplitude B_1, 13 ms before the c.w. sequence. During this pulse, $\mathbf{M}_0$ rotates about $\mathbf{B}_{\rm e}$ through an angle φ. The angle obtained at the end of the pulse is $\varphi = \gamma|\mathbf{B}_{\rm e}|\tau_{\rm p}$ [15,17]. Within a few milli-seconds after the pulse, the nutated magnetization vector decays to its longitudinal component which then determines the amplitude of the maximum vibrations achieved by the cantilever during the force measurement. B_1 is set at maximum power, *i.e.* 6.4 W, for the pulse. The c.w. sequence uses a 2.9 W r.f. field. Figure 4 shows

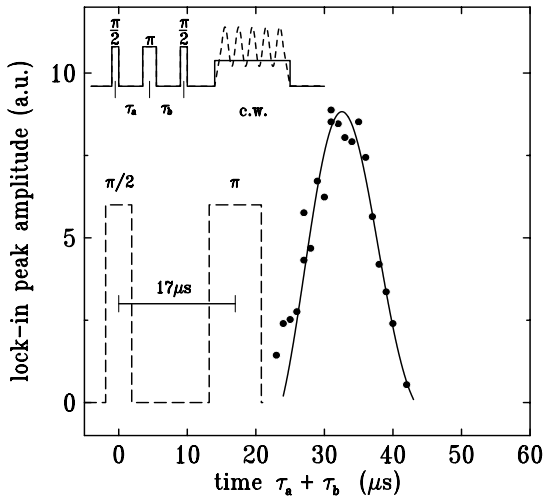

Fig. 5. Measurement of the transient shape of the spin-echo: a $\pi/2$-τ_a-π pulse sequence is used to form a spin echo. The transverse magnetization is measured with the combination of a $\pi/2$ pulse and the c.w. sequence. The amplitude of the force signal is shown as a function of $\tau_a + \tau_b$ with a fixed $\tau_a = 17$ μs. A r.f. field of $B_1 = 15$ G is used for the pulses. The settings for the c.w. sequence are a r.f. field of 10 G, $\Omega/2\pi = 50$ kHz and $\tau_l = 100$ ms. The solid line is the calculated shape of the spin echo expected for a platelet of 6.5 μm thickness in the inhomogeneous magnetic field.

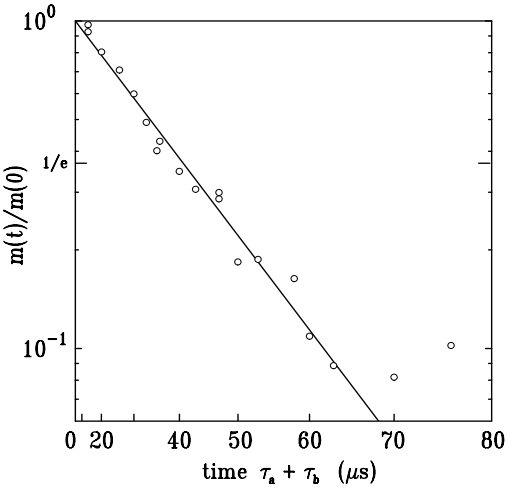

Fig. 6. Spin-spin relaxation time measurement: normalized heights of the spin echo are displayed on a square-logarithmic scale as a function of $\tau_a + \tau_b$ with $\tau_a = \tau_b$. The straight line is a fit with $\exp\left\{-(2\tau_a/T_2)^2\right\}$ where $T_2 = 39 \pm 1$ μs.

the lock-in output averaged over a 1 s time interval around its peak amplitude. For spins that are at ζ_0, the signal is proportional to $\cos\varphi$. The data are fitted by the functional form $\exp(-\tau_p/\tau)\cos(\gamma B_1 \tau_p) + b$. The period gives a calibration of the r.f. field strength at the sample location and we get $B_1 = 15$ G during the pulse. The other fitting parameters are $\tau = 43 \pm 6$ μs and a positive offset $b = 3 \pm 0.2$ Å. The values of these last two parameters depend strongly on B_1. The positive offset b is mainly due to the non-uniform field inside the sample [33]. For ^{1}H away from ζ_0, the direction of $\mathbf{B}_e$ is not exactly perpendicular to $\mathbf{k}$ and only a partial inversion of the z component is obtained when $\varphi = \pi$. The decay of the magnetic moment fitted by τ is due to field inhomogeneity which causes a dephasing of the magnetization in the transverse plane [34].

To study the transverse magnetization decay of ^{1}H [17] a sequence of 3 pulses is used. A $\pi/2$ pulse is applied to the spin system, so that the magnetization at ζ_0 is rotated to the transverse plane. After a fixed delay, τ_a, a π pulse is applied to form a spin echo. Shortly after, a $\pi/2$ pulse takes an instant snap-shot of the transverse magnetization by rotating it along $\mathbf{k}$ and the frozen component is measured with the c.w. sequence. Varying the time delay, τ_b, between the last two pulses reconstructs the transient shape of the spin echo. Using the same settings as the earlier measurement, the widths of the $\pi/2$ and π pulse are set to 3.8 μs and 7.6 μs respectively. The delay between the center of the first two pulses is $\tau_a = 17$ μs. In Figure 5, the lock-in peak (again averaged over 1 s around its maximum) is shown as a function of $\tau_a + \tau_b$. As expected for a spin echo, the reconstructed transverse magnetization becomes refocused at a time $2\tau_a$. The shape of the spin echo reflects mainly the inhomogeneous broadening of the resonance line as due to the strong field gradient. The amplitude, however, should only be affected by the homogeneous contributions to the ^{1}H line (dipolar coupling).

With increasing spacing τ_a between pulses, the size of the spin echo signal decreases due to spin-spin relaxation. Using the same sequence as above, Figure 6 is a plot of the spin echo amplitude measured as a function of the time $2\tau_a$. The measured values are plotted on a x^2-log(y) scale and one finds that the data follow the relationship $\exp\left\{-(t/T_2)^2\right\}$ with $T_2 = 39 \pm 1$ μs. Taking the inferred T_2, the dipolar linewidth [28] and the inhomogeneous broadening as due to the field gradient, the shape of the echo in Figure 5 is simulated. The solid line in Figure 5 is the best fit obtained for a sample thickness of 6.5 μm which is in good agreement with the value obtained on the image.

The longitudinal magnetization recovery is now measured after a saturation comb [35]. This protocol puts efficiently inhomogeneous spin systems in a well defined uniform state outside thermal equilibrium. The saturation comb is composed of three $\pi/2$ pulses spaced by 100 μs. The c.w. sequence is applied at a variable delay (13 ms $< t <$ 20 s) after the comb. In order to obtain an intrinsic measurement of the relaxation, it is important to ensure that the sensitivity profile $a_1(\zeta)$ is exclusively included inside the sample section, otherwise a partial repolarization of the magnetization occurs during the measurement cycle [17]. For our settings, ζ_0 is set exactly at the middle of the sample and $\Gamma = 2.4$ μm is smaller than the sample thickness. As before, the value plotted is the lock-in output averaged over a 1 s time interval around its maximum. No signals are detected when $t = 13$ ms.

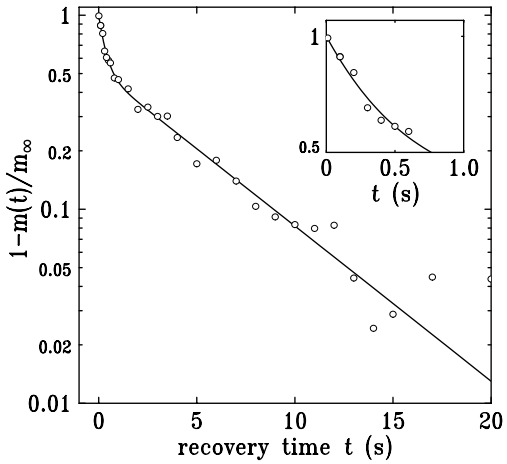

Fig. 7. Measurement of the longitudinal magnetization recovery: the logarithmic of the normalized amplitude of the force signal is shown as a function of the interval t between a saturation comb and the c.w. sequence. The solid line is a fit with a double exponential recovery which yields $T_{1s} = 0.35 \pm 0.03$ s and $T_{1l} = 5.4 \pm 0.5$ s. Each point is the average of 32 c.w. sequences. A r.f. field of $B_1 = 15$ G is used for the comb. The settings for the cyclic adiabatic inversions are a r.f. field of 7 G, $\Omega/2\pi = 50$ kHz and $\tau_1 = 100$ ms. We make sure that there is no net repolarization of M during the c.w. sequence.

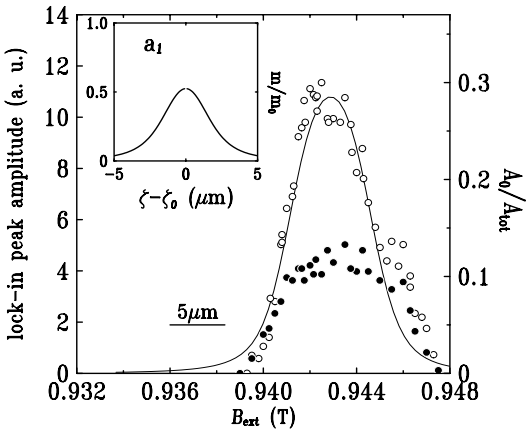

Fig. 8. Force signal as a function of $B_{\rm ext}$: a saturation comb is applied 0.6 s (closed circles) and 16 s (open circles) before the c.w. sequence. The solid line is the expected profile for a parallelepiped sample of 7 μm thickness within both the free spin and adiabatic approximations. The c.w. sequence uses a r.f. field of 7 G, $\Omega/2\pi = 25$ kHz and $\tau_1 = 300$ ms. The inset shows the transfer function that corresponds to these settings, a_1 is the spatial dependence of the sensitivity profile.

In Figure 7, two relaxation times in the recovery process are clearly observed. The results are fitted with a double exponential $\varrho_s \{1 - \exp(-t/T_{1s})\} + (1 - \varrho_s) \{1 - \exp(-t/T_{1l})\}$ which gives $\varrho_s = 49 \pm 2\%$, $T_{1s} = 0.35 \pm 0.03$ s and $T_{1l} = 5.4 \pm 0.5$ s. The value ϱ_s does not correspond directly to the proportion of spins that have a short relaxation (n_s) since the factor between M_z and the lock-in amplitude is also a function of T_1.

Neutron diffraction studies [36] of the $(NH_4)_2SO_4$ crystal structure show that there are two NH_4^+ sites at room temperature surrounded respectively by five and six SO_4^{2-} ions. The protons of the two inequivalent ammonium ions are coupled *via* dipole-dipole interactions and the measured spin-lattice relaxation rate at 300 K is an averaged value of the T_1^{-1}. In a variable temperature NMR measurements, O'Reilly and Tsang [23] observe a single exponential ^{1}H relaxation process and analyze their T_1 results by the reorientation correlation times τ_0 of the two distinctive NH_4^+. At 300 K, $1/\tau_0$ should be larger than the Larmor frequency and the rotation should be isotropic which means that T_1 should be independent of the orientation between the static field and the crystallographic axis. We suppose that our observed two T_1 processes might be due to water contamination inside the sample during its contact with air. The presence of H_2O in the crystal lattice could decrease the reorientation correlation time of the ammonium ions, hence diminishing the protons T_1. The relatively high proportion of spins with short T_1 might be due to the exceptionally small thickness of our crystal (7 μm).

In order to check the latter hypothesis, a conventional NMR measurement was performed by A. Dooglav with a 1 T custom spectrometer. The sample consisted of ~ 1 g of our sample ground to small particles with dimensions below 50 μm. In this fine powder sample, a double relaxation process is also observed with the following parameters $n_s = 17 \pm 5\%$, $T_{1s} = 0.37 \pm 0.1$ s and $T_{1l} = 4.7 \pm 0.2$ s. This result is in sharp contrast with experiments performed on coarser grains, where only one relaxation is observed with $T_1 = 5.0 \pm 0.2$ s. The values of the two relaxation times are equal, within error bars, to the ones measured by MRFM. In addition, measurements were performed on the same 50 μm powder after two weeks of aging in air. It showed a rise of n_s to $26 \pm 3\%$ in the longitudinal magnetization recovery experiment. A standard spin-spin relaxation measurement on this powder seems also to indicate a double time T_2 with $n_s = 20 \pm 6\%$, $T_{2s} = 49 \pm 12$ μs and $T_{2l} = 79 \pm 1$ μs.

One corollary issue concerns the spatial distribution of each spin species inside the sample section. To perform this measurement, we record the amplitude of the lock-in signal as a function of $B_{\rm ext}$. By sweeping $B_{\rm ext}$, the surface ζ_0 is displaced to different heights in the sample. The force signal is then proportional to the density of spin around this location. In order to obtain a local measurement, the thickness Γ of the slice probed is reduced by decreasing both Ω and B_1. The inset of Figure 8 shows the spatial dependence of the transfer function $a_1(\zeta)$ for our settings and Γ, the half width at half maximum, is 1.9 μm. Figure 8 shows the amplitude of the lock-in signal obtained for two different delays t between the saturating comb and the c.w. sequence. By changing t, the weight ϱ_s of one spin species compared to the other is varied. Qualitatively, this protocol gives more weight to the spin species with short relaxation when the comb is close to the c.w. sequence. A first look at the result indicates that a more rounded distribution is obtained for the $t = 0.6$ s data.

The measurements, however, collected close to the edge of the sample are skewed by repolarization processes that modify the shape of the lock-in signal. Inside the bulk of the crystal (0.942 T $\lesssim B_{\rm ext} \lesssim$ 0.944 T), there is no clear evidence of a spatial modulation of one spin population compared to the other, *e.g.* a dip of the signal at 0.9425 T, the middle of the crystal. This result suggests that, within our resolution, the water contamination is uniform in the thickness. The solid line is a calculation of the expected profile for a parallelepiped sample of dimensions $100 \times 50 \times 7$ μm^3 within both the free spin and adiabatic approximations. In spite of the idealized model, the $t = 16$ s data (open circles) are well described by the calculated profile, except for the high-field range. The shoulder at $B_{\rm ext} = 0.946$ T corresponds to the surface of the sample that has been glued with epoxy to the cantilever. We did not attempt to fit this part of the data. The observed step in the signal might be due to the protons in the epoxy. A small roll angle between the sample and the cantilever combined with the particular shape of our crystal is also consistent with the observed effect.

Although the data analyzed here-above ensure that two populations of spin with different NMR properties are present, their actual proportion is not quantitatively determined, as the actual values of the relaxation times influence the magnitude of the measured signal. For a better knowledge of the sensitivity of the technique to the measurement parameters, it is then necessary to perform quantitative analyses.

4 Quantitative measurements

In this section, we shall first calibrate the mechanical response of the cantilever and the mechanical noise. The time dependence $A(t)$ of the lock-in signal is calculated, taking into account relaxation processes and non-adiabatic effects. The experimental responses for different values of B_1 and Ω are compared with the calculations. This allows us to select an experimental condition for which non-adiabatic effects can be neglected. It is then shown that two relaxation times are indeed required to fit the time dependence of the observed lock-in signals, with values consistent with those obtained from T_1 data.

The Q of the cantilever is first measured carefully using the noise vibration spectrum of the cantilever loaded with the sample in vacuum when the r.f. power is off. The lock-in time constant is set to $\tau_{\rm l}$= 10 s. An audio generator sweeps the lock-in reference around $\omega_{\rm c}$. The plotted value in Figure 9 is the standard deviation of the lock-in signal estimated over $100\times\tau_{\rm l}$ (the mean lock-in signal is zero). During the whole experiment, the temperature stability of the cantilever is better than $\pm$0.01 °C which guarantees that $\omega_{\rm c}$ does not shift by more than 0.01 Hz. Fitting the squared amplitude with a Lorentzian [37], one obtains the cantilever resonance frequency $\omega_{\rm c}/2\pi = 1\,397.77$ Hz and quality factor $Q = 4\,000$ (defined as the ratio of $\omega_{\rm c}$ over the full width at half maximum of the *power* spectrum). Away from resonance, our sensitivity is limited

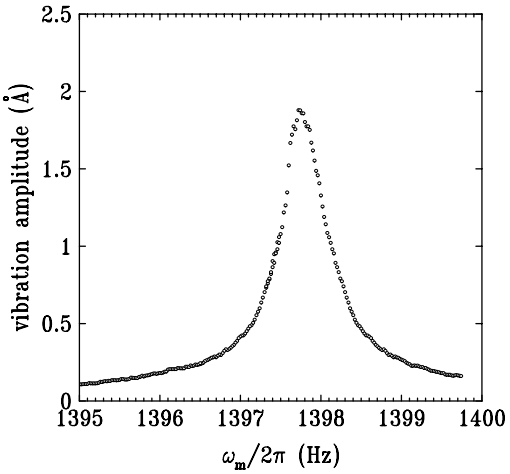

Fig. 9. Noise vibration spectrum of the cantilever with the sample attached: the data is obtained in vacuum (10^{-2} torr) when *no* r.f. fields are applied. The lock-in time constant is $\tau_{\rm l}$= 10 s. The signal is the standard deviation of the lock-in output estimated over $100\times\tau_{\rm l}$. The cantilever holder temperature stability is better than $\pm$0.01°C during the measurement.

by the noise of the detection electronics. It is several orders of magnitude smaller than the Å-scale motion of the cantilever at resonance and therefore it can be neglected. Near $\omega_{\rm c}$, the cantilever motion consists of white noise amplified by a narrow-bandwidth mechanical resonator [38]. $\Delta\nu_{\rm c}$ is the one-sided equivalent noise bandwidth (ENBW) of the mechanical resonator $\Delta\nu_{\rm c} = \omega_{\rm c}/8Q = 0.27$ Hz. The noise at the output of the lock-in is this narrow-band motion noise observed through a RC filter of time constant $\tau_{\rm l} = 1/RC$ whose ENBW $\Delta\nu_{\rm l} = 1/4\tau_{\rm l} = 0.025$ Hz. Exactly at resonance, the combined distribution gives an ENBW $\Delta\nu = (1/\Delta\nu_{\rm c} + 1/\Delta\nu_{\rm l})^{-1} = 0.023$ Hz. To convert our data to spectral density, the resonance amplitude in Figure 9 must be divided by $\sqrt{\Delta\nu}$. The measured noise spectral density is $\mathcal{A} = 13$ Å$/\sqrt{\rm Hz}$. This figure also corresponds to the noise observed in Figure 3 where $\Delta\nu = 0.20$ Hz. The result has to be compared with the intrinsic correlation function for fluctuations of a Brownian particle harmonically bound to an oscillator with a single degree of freedom of spring constant k:

$$\langle AA(t)\rangle = \frac{4Qk_{\rm B}T}{k\omega_{\rm c}}\cdot \tag{5}$$

Taking the square root of the above expression, one gets $\mathcal{A}_T = 10$ Å$/\sqrt{\rm Hz}$ at $T = 300$ K which is in good agreement with our measured value. In conclusion, our dominant noise comes from the thermal vibration of the cantilever. From this result, one can estimate the smallest force detectable by the instrument in one shot $k\mathcal{A}/Q = 2\times10^{-15}N/\sqrt{\rm Hz}$.

In order to obtain a quantitative measurement of our force signal when the r.f. field is applied, a more detailed study of the time dependence of the lock-in signal $A(t)$ is needed. The length of the c.w. sequence is increased

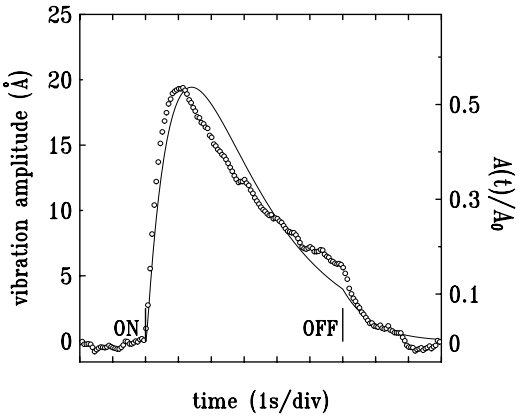

Fig. 10. Time dependence of the lock-in signal: the trace is the average of 32 c.w. sequences with $\tau_\mathrm{l} = 30$ ms. The c.w. sequence is composed of a r.f. field of 10 G with $\Omega/2\pi = 50$ kHz. The solid line is the calculated vibration amplitude of a harmonic oscillator driven by a damped sinusoidal magnetic force with a decay time constant $\tau_\mathrm{m} = 2.2 \pm 0.07$ s. In this case, the predicted maximum signal is $A_\mathrm{peak} = 0.5A_0$ with $A_0 = QF_0/k$.

to 6 s compared to Figure 3. Figure 10 is the average of the lock-in signal over 32 sequences using a short lock-in time constant of $\tau_\mathrm{l} = 30$ ms. The striking feature of this plot is that the norm of the magnetization $|\mathbf{M}|$ decays during the c.w. sequence. We have checked that experimental perturbations such as the phase noise of the r.f. source are negligible in this case [39].

In the rotating frame, the magnetization tends to recover slowly towards a steady state value due to spin-lattice relaxation processes [40]. These relaxations are different from the ones measured in section 3 which are inferred from the time evolution of the magnetization in the *absence* of r.f. fields. In addition, the lack of adiabaticity quantified by $\alpha \approx \dot{\theta}/\gamma B_\mathrm{e}$ produces a precession movement around the locally changing effective field direction. This mistracking corresponds to a magnetization component perpendicular to the instantaneous precession axis $\mathbf{B}_\mathrm{e} + \dot{\theta}/\gamma\,\mathbf{j}$ that relaxes due to spin-spin interactions. But in the limit $\alpha \ll 1$ and $2\pi/\omega_\mathrm{m} \ll T_1$, the decrease of M after one cycle $\Delta = M(t + 2\pi/\omega_\mathrm{m}) - M(t)$ is small. The value is calculated at the lowest order for one spin species (see Appendix B).

$$\begin{aligned}\Delta \approx -M \Bigg\{ & \int_0^{\frac{2\pi}{\omega_\mathrm{m}}} \dot{\theta}(t) \int_0^t \dot{\theta}(t') \exp\left(-\int_{t'}^t \frac{1}{T_1^+}\mathrm{d}t''\right) \\ & \times \cos\left(\int_{t'}^t \frac{\gamma B_1}{\sin\theta(t'')}\mathrm{d}t''\right)\mathrm{d}t'\mathrm{d}t \\ & + \int_0^{\frac{2\pi}{\omega_\mathrm{m}}} \left(\frac{\cos^2\theta(t)}{T_{1z}} + \frac{\sin^2\theta(t)}{T_{1x}}\right)\mathrm{d}t \Bigg\} \\ & + M_0 \int_0^{\frac{2\pi}{\omega_\mathrm{m}}} \frac{\cos\theta(t)}{T_{1z}}\mathrm{d}t, \end{aligned} \tag{6}$$

where T_{1z} is the usual T_1 in the absence of an r.f. field, T_{1x} is the transversal spin-lattice relaxation and $1/T_1^+ = (1/T_{1y} + \cos^2\theta/T_{1x} + \sin^2\theta/T_{1z})/2$. It was shown that the relaxation mechanisms in this compound are associated with the time varying field induced by the change in the NH_4^+ orientation. For an exponential correlation function with correlation time τ_0, T_{1x} is expressed as a sum of the spectral density of these fluctuating fields $J^{(i)}(\omega) = \tau_0/(1+\omega^2\tau_0)$ with an index i that corresponds to the number of net spin flip: $1/T_{1x} = \frac{3}{2}\gamma^4\hbar^2 I(I+1)/r^6(\frac{5}{2}J^{(1)}(\omega_0) + \frac{1}{4}J^{(2)}(2\omega_0) + \frac{1}{4}J^{(0)}(2\omega_\mathrm{e}))$, with $\omega_\mathrm{e} = \gamma B_\mathrm{e}$. In the approximation for our compound that $\omega_\mathrm{e}\tau_0 \ll 1$, one obtains that T_{1x} is independent of θ and $T_{1y} = T_{1x}$. Coming back to equation (6), one recognizes that the first integral is the decrease due to the finite value of the non-adiabaticity parameter α (see Appendix B). The second represents the spin-lattice relaxation $T_{1\rho}$ in the rotating frame [41]. The last integral is the equilibrium magnetization that corresponds to the spin temperature in the rotating frame. τ and M_eq are defined by rewriting the above expression in the form $\Delta/2\pi = -M/(\omega_\mathrm{m}\tau) + M_\mathrm{eq}/(\omega_\mathrm{m}\tau)$. During the c.w. sequence, the oscillatory driving magnetic force is dampened and the instantaneous value is given by:

$$F(t) \approx g\sin(\omega_\mathrm{m}t)\int_{V_\mathrm{s}} a_1(\zeta)\,M(\zeta,t)\,\mathrm{d}\zeta + \text{const.}, \tag{7}$$

with

$$M(\zeta,t) = \left\{ M_\mathrm{eq}(\zeta) + \{M_0 - M_\mathrm{eq}(\zeta)\}\exp\left(\frac{-t}{\tau(\zeta)}\right)\right\}. \tag{8}$$

The integral in equation (7) relaxes approximately according to a single exponential towards its equilibrium value $m_\mathrm{eq} = \int_{V_\mathrm{s}} a_1(\zeta)M_\mathrm{eq}(\zeta)\mathrm{d}\zeta$ with an apparent characteristic time τ_m. One notes that $m_\mathrm{eq} = 0$ by symmetry when ζ_0 is centered at the middle of the sample $\zeta_0 = \zeta_\mathrm{m}$. The value of m_eq is positive for $\zeta_0 < \zeta_\mathrm{m}$ and changes sign for $\zeta_0 > \zeta_\mathrm{m}$ [17]. In the particular case where $m_\mathrm{eq} = 0$ and $\alpha \ll 1$, then it can be shown that the coefficient τ_m is bounded between $T_{1x} \leq \tau_\mathrm{m} \leq T_{1z}$ [21].

The forced vibrations of an harmonic oscillator are given by the convolution product:

$$a(t) = \beta\int_0^t \frac{F(t')}{k}\exp\left\{-\frac{t-t'}{\tau_\mathrm{c}}\right\}\sin\{\omega_\mathrm{c}(t-t')\}\;\omega_\mathrm{c}\,\mathrm{d}t', \tag{9}$$

with $\beta = \left\{1 + 1/(4Q^2)\right\}$ and $1/\tau_\mathrm{c} = \frac{1}{2}\omega_\mathrm{c}/Q$ the damping constant of the cantilever. In our experiment the external force is $F(t) = F_0\exp(-t/\tau_\mathrm{m})\exp(\mathrm{i}\omega_\mathrm{m}t)$ for $m_\mathrm{eq} = 0$, with $F_0 = kA_0/Q$ and τ_m the characteristic decay time of the magnetic force. $a(s)$ the Laplace transform of equation (9) is calculated in the complex plane:

$$\frac{k}{F_0}a(s) = \frac{\tau_\mathrm{m}\left(4Q^2+1\right)}{(s\tau_\mathrm{m} + 1 - \mathrm{i}\tau_\mathrm{m}\omega_\mathrm{m})\left\{(s\tau_\mathrm{c}+1)^2 + 4Q^2\right\}}\cdot \tag{10}$$

The response $A(t)$ of the lock-in is the imaginary part of the inverse Laplace transform $\mathcal{L}^{-1}\left\{a(s + \mathrm{i}\omega_\mathrm{m})/(1 + \tau_\mathrm{l}s)\right\}$

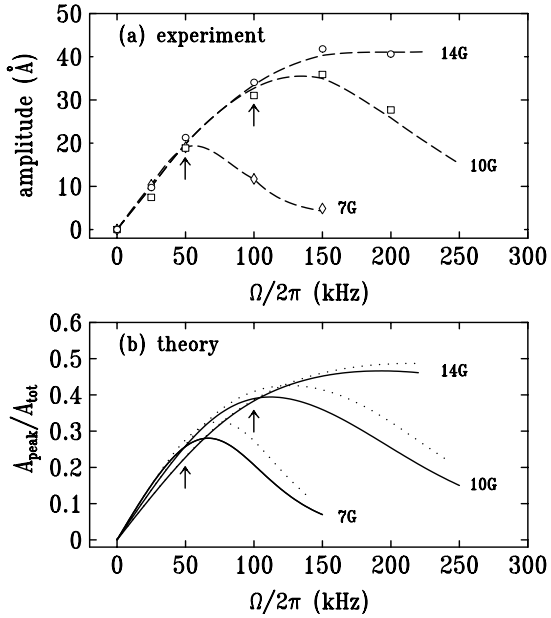

Fig. 11. (a) Measurements of the amplitude of the lock-in signal is shown as a function of the modulation amplitude for different strengths of the r.f. field. The dashed lines are guides for the eye. The arrows indicate the limits of the adiabatic regime. The measurements are performed at $B_{\rm ext} = 0.9425$ T. (b) Calculated amplitude of the lock-in signal obtained for a 7 μm thick sample using equation (7). The parameters introduced in the model are $T_{1z} = 4.9$ s, $T_{1x} = T_{1y} = 3.2$ s and $T_2 = 40$ μs (solid line) or 100 μs (dotted line).

with $\tau_{\rm l}$ the lock-in time constant. An approximation can be obtained in the special case where $\omega_{\rm m} = \omega_{\rm c}$ in the limit $Q \gg 1$ and $\omega_{\rm c} \gg (1/\tau_{\rm m}, 1/\tau_{\rm l})$.

$$\frac{A(t)}{A_0} \approx \frac{1}{(1/\tau_{\rm m} - 1/\tau_{\rm c})(\tau_{\rm c} - \tau_{\rm l})} \exp\left(-\frac{t}{\tau_{\rm c}}\right) + \frac{\tau_{\rm m}/\tau_{\rm c}}{(1/\tau_{\rm c} - 1/\tau_{\rm l})(\tau_{\rm l} - \tau_{\rm m})} \exp\left(-\frac{t}{\tau_{\rm l}}\right) + \frac{\tau_{\rm m}/\tau_{\rm c}}{(1/\tau_{\rm c} - 1/\tau_{\rm m})(\tau_{\rm m} - \tau_{\rm l})} \exp\left(-\frac{t}{\tau_{\rm m}}\right). \quad (11)$$

The sum of these three exponentials vanishes at $t = 0$ and each term decays to zero with a different time constant at a later time $t > 0$. This leads to a peaked lock-in signal whose amplitude $A_{\rm peak}$ and position depends on $\tau_{\rm m}$ (for a fixed $\tau_{\rm c}$ and $\tau_{\rm l}$). At the end of the c.w. sequence in Figure 10 ($t > 6$ s), the decaying free oscillations of the cantilever (time constant $\tau_{\rm c}$) are observed. If one tries to fit the data with the above nonlinear form, $\tau_{\rm m} = 2.2 \pm 0.07$ s is obtained but the quality of the fit is not very good. Values of $\tau_{\rm m}$ smaller than $T_{1x} = 3.2$ s have also been reported by Verhagen *et al.* [21] and these findings were attributed to the phase noise of the r.f. source. However, when large modulation amplitudes are employed for the c.w. sequence, such a fast force decay can also be consistent with a magnetization decrease due to a lack of adiabaticity.

To understand further the meaning of this fit parameter $\tau_{\rm m}$, we plot in Figure 11a the lock-in peak amplitude measured for different values of Ω and B_1 when $B_{\rm ext} = 0.9425$ T. The non-adiabaticity parameter α increases along the abscissa axis. For a fixed Ω and B_1, the value of α oscillates with time and passes through a maximum, $\alpha_{\rm max} = \Omega\omega_{\rm m}/(\gamma^2 B_1^2)$, at a time $t = 0$ modulo $\pi/\omega_{\rm m}$. Figure 11b shows the amplitude of the peak signal $A_{\rm peak}$ predicted by equation (11) with $F(t)$ calculated from equation (7) using a sample thickness of 7 μm. The results are normalized by $A_{\rm tot} = QgM_0V_{\rm s}/(k\sqrt{2})$ the amplitude associated with a uniform inversion of all spin inside the sample. The parameters introduced in the model are the values of the spin-lattice relaxation times measured on powder samples by conventional NMR with $T_{1z} = 4.9$ s along the static field and $T_{1x} = 3.2$ s along a 10 G r.f. field, in the approximation that $T_{1y} = T_{1x}$. In our theoretical model, perturbation effects from the dipolar broadening are also introduced. They are approximated as a time independent local field with a Lorentzian lineshape. The solid lines are the numerical predictions using $T_2 = 40$ μs and the dotted lines correspond to $T_2 = 100$ μs.

The increase of the force signal at small $\Omega(\leq 50$ kHz) corresponds to an increase of the modulated magnetic moment. Larger frequency deviation increases the width of the probed slice, Γ, and more protons oscillate at $\omega_{\rm m}$. For both large $B_1 \geq 14$ G and large $\Omega \geq 150$ kHz the amplitude of the signal eventually saturates when Γ becomes greater than the sample thickness.

For $B_1 = 7$ and 10 G, the deviation from the low Ω-linear increase (indicated by the arrows) marks the cross-over from an adiabatic regime to a quasi-adiabatic one [40]. In our sample the threshold occurs at $\alpha_{\rm max} = 0.1$, in good agreement with the theoretical model. In the adiabatic regime ($\alpha_{\rm max} < 0.1$) the dominant relaxation processes, which reflect in $\tau_{\rm m}$, correspond to $T_{1\rho}$ effects, while, in the quasi-adiabatic regime ($\alpha_{\rm max} > 0.1$), they result from dipolar interactions with a ratio determined by the non-adiabaticity parameter ($T_2 < \tau_{\rm m} < T_1$, see Appendix B). The predicted position of this cross-over depends somewhat on the dipolar contribution T_2.

From the last discussion, one can conclude that the settings of Figure 10 correspond to a non-adiabatic parameter $\alpha_{\rm max} = 0.04$ well inside the adiabatic regime for our compound. It can then be inferred that the decrease of the force signal in Figure 10 is due to spin-lattice effects in the rotating frame and our fitted value of $\tau_{\rm m}$ must be an average of the two T_1's reported in Figure 7.

The time dependence of the lock-in signal is fitted with a double damped synchronous excitation of *two* spin populations with respectively short ($\tau_{\rm ms}$) and long ($\tau_{\rm ml}$) relaxation times. The nonlinear function $n_{\rm s}A(t, \tau_{\rm ms}) + (1 - n_{\rm s})A(t, \tau_{\rm ml})$ is used where $A(t)$ is given by equation (11). The best fit is obtained for $\tau_{\rm ms} = 0.55 \pm 0.02$ s, $\tau_{\rm ml} = 4.8 \pm 0.2$ s and $n_{\rm s} = 69 \pm 1\%$. The result is the solid line shown in Figure 12. The fit values obtained for the relaxation times are similar to those measured in the magnetization recovery experiment in Figure 7. An immediate question is which portion of the lock-in output signal

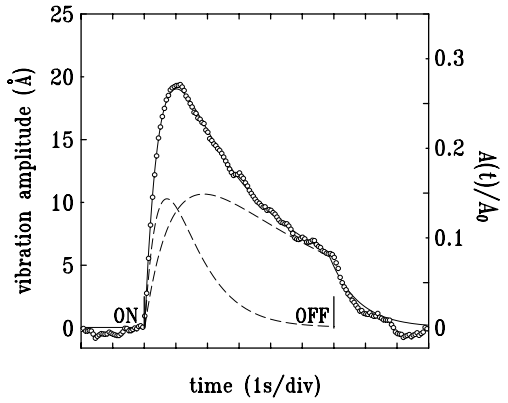

Fig. 12. Signal of Figure 10: the solid line is the response of an harmonic oscillator driven by two synchronous forces with short and long relaxations times $n_{\rm s}A(t,\tau_{\rm ms})+(1-n_{\rm s})A(t,\tau_{\rm ml})$. The best fit is obtained for $\tau_{\rm ms}=0.55\pm0.02$ s, $\tau_{\rm ml}=4.8\pm0.2$ s and $n_{\rm s}=70\%$. The height of the peak is $0.3A_0$. The dashed lines show the contribution of each spin species.

should be used when several spin species are present in the sample. In Figure 12 the separate contribution to the lock-in signal of each spin species (dashed lines) is shown. The maximum force signal of the two spin species occurs respectively 0.7 s and 1.9 s after the start of the c.w. sequence for the short and long $\tau_{\rm m}$. We recall that our definition of the force signal is the average of the lock-in peak amplitude over a 1 s time interval around its maximum value. This approach gives approximately equal weights to both spin species in the measurement. One can also observe in Figure 12 that the height of the two peaks are approximately equal despite the fact that there is 2.3 times more spin with short relaxation. As a matter of fact it can be shown that the mechanical detection is 2.4 times more sensitive to the spins that have a 4.8 s relaxation time compared to the spins that have a 0.55 s one. From this result, the value of the fit parameter $\varrho_{\rm s}\approx0.5$ in Figure 7 can be converted into the proportion of spins that have a short relaxation $n_{\rm s}=2.4\varrho_{\rm s}/\{(2.4-1)\varrho_{\rm s}+1\}=70\%$; a value that agrees well with the fit $n_{\rm s}$ in Figure 12.

Finally, the expected amplitude of the force signal for our sample is calculated. Using equation (4), one gets a value of $A_0=100$ Å for the settings used in Figure 12 ($B_1=10$ G and $\Omega/2\pi=50$ kHz). In Figure 12 the predicted amplitude of the lock-in peak is $0.3A_0$, or 30 Å, which is close to the experimentally measured value of 20 Å. In conclusion, our measured amplitude of the peak lock-in signal is in good agreement with the theoretical prediction if the two spin-lattice relaxation times of the two spin species are taken into account. Other effects such as misalignment of the sample compared to the cylinder magnetic axis can account partially for a decrease of the signal (*e.g.* an offset of 0.1 mm from the axis decreases the amplitude of the lock-in signal by a factor of 2).

5 Conclusion

Measurement sequences combining fast adiabatic passages and pulses have been reported. They allow us to measure T_1 and T_2 for microscopic samples using a mechanical detection. This has been applied to quantitative analyses of the detected signals for a 7 μm thick sample of $(NH_4)_2SO_4$. The transverse relaxation T_2 has been found consistent with conventional NMR detection on a macroscopic sample. Our sample displays, however, two spin lattice relaxation times $T_{1\rm s}=0.4$ s and $T_{1\rm l}=5$ s. While the long $T_{1\rm l}$ corresponds to that measured for coarse powder samples, the short $T_{1\rm s}$ might be due to water contamination of our thin crystal during its contact with air. This contamination is found to be uniform in the thickness of the sample. This large difference in T_1 values has allowed us to study the influence of the spin-lattice relaxation in the rotating frame on the time dependence of the lock-in signal, as well as the variation of signal intensity with increasing non-adiabaticity of the sweep sequence. A consistent analysis of all experimental parameters has been proposed and will be quite useful in future quantitative investigations of MRFM signals. Our work also raises the problem of how to perform reliable spin lattice relaxation measurements at the sample surface. Our T_1 investigation is mainly restrained to the bulk of the sample, because the shape of the lock-in signal (which reflects in the apparent relaxation times) varies with $B_{\rm ext}$. These difficulties prevented us from interpreting quantitatively our results on the spatial distribution of the different spin densities close to the edge. These issues will be best solved by performing a similar experiment on a hetero-layer sample of well-characterized composition.

We are greatly indebted to A. Dooglav for his help in the conventional NMR experiments. We also would like to thank C. Fermon, M. Goldman, J.F. Jacquinot and G. Lampel for stimulating discussions. This research was partly supported by the Ultimatech Program of the CNRS.

Appendix A: Inhomogeneous field

Near the axis, a uniformly magnetized ($M_{\rm s}$) cylinder of length l and diameter ϕ produces a field, whose component along $\mathbf{k}$, $B_{\rm cyl}$, decays radially as

$$\frac{B_{\rm cyl}(r,z)}{4\pi M_{\rm s}}=\left\{b_{\frac{1}{2}}\left(\frac{z+l}{\phi}\right)-b_{\frac{1}{2}}\left(\frac{z}{\phi}\right)\right\}$$
$$+3\left\{b_{\frac{5}{2}}\left(\frac{z+l}{\phi}\right)-b_{\frac{5}{2}}\left(\frac{z}{\phi}\right)\right\}\frac{r^2}{\phi^2}+\mathcal{O}(r^4),\quad\text{(A.1)}$$

with $b_a(z)=z\left(1+4z^2\right)^{-a}$. The fields are expressed in cylindrical coordinates with the origin centered on the cylinder's upper surface (see Fig. 1). In our case $M_{\rm s}$ is calculated from the applied field $B_{\rm ext}$ needed to produce a resonance signal at the sample position, $z=0.70$ mm. $B_{\rm cyl}(0,z=0.70)=\omega_0/\gamma-B_{\rm ext}=0.352$ T is put in the above expression and one obtains $M_{\rm s}\approx1400$ emu/cm^3 for our iron. Using this result, the gradient $g=-470$ T/m at the sample location is calculated.

Appendix B: Adiabaticity

The aim of this Appendix B is to calculate the decrease of the magnetization due to the spin-lattice relaxation and the lack of adiabaticity. The solution below is proposed by M. Goldman. In the limit of strong r.f. fields (larger than the local field), one can neglect the spin-lattice relaxation of the dipolar energy expectation value. In the rotating frame, the time evolution of the different spin components are [40]:

$$\frac{\partial\langle I_z\rangle}{\partial t} = -\gamma B_1\langle I_y\rangle + \frac{\langle I_0\rangle - \langle I_z\rangle}{T_{1z}} \tag{B.1a}$$

$$\frac{\partial\langle I_x\rangle}{\partial t} = +\gamma B_1\cot\theta\langle I_y\rangle - \frac{\langle I_x\rangle}{T_{1x}} - \frac{\mathrm{i}}{\hbar}\langle[\mathcal{H}_{\mathrm{D}z}, I_x]\rangle \tag{B.1b}$$

$$\frac{\partial\langle I_y\rangle}{\partial t} = +\gamma B_1\left(\langle I_z\rangle - \cot\theta\langle I_x\rangle\right) - \frac{\langle I_y\rangle}{T_{1y}} - \frac{\mathrm{i}}{\hbar}\langle[\mathcal{H}_{\mathrm{D}z}, I_y]\rangle, \tag{B.1c}$$

with $\langle\mathbf{I}\rangle = \mathrm{Tr}(\mathbf{I}\sigma)$ the expectation value of the magnetization, σ the instantaneous density matrix in the rotating frame and $\mathcal{H}_{\mathrm{D}z}$ the secular part of the dipolar Hamiltonian. The commutator incorporates the local field contribution defined through $B_{\mathrm{L}}^2 = \mathrm{Tr}(\mathcal{H}_{\mathrm{D}z}^2)/\gamma^2\mathrm{Tr}(I_z^2)$. In our notation θ is the angle between the directions of the static and effective field, $B_{\mathrm{e}} = B_1/\sin\theta$, with $B_1\cot\theta$ the projection along $\mathbf{k}$. Under r.f. irradiation, a new coordinate system $\{X, Y, Z\}$ is defined through a transformation by the unitary operator $\exp(-\mathrm{i}\theta I_y)$, a rotation around y by θ. In the doubly rotating frame the differential equations then become:

$$\frac{\partial\langle I_Z\rangle}{\partial t} = +c\frac{\langle I_0\rangle}{T_{1z}} - \left\{\frac{s^2}{T_{1x}} + \frac{c^2}{T_{1z}}\right\}\langle I_Z\rangle + \left(\dot\theta - cs\left\{\frac{1}{T_{1x}} - \frac{1}{T_{1z}}\right\}\right)\langle I_X\rangle \tag{B.2a}$$

$$\frac{\partial\langle I_X\rangle}{\partial t} = -s\frac{\langle I_0\rangle}{T_{1z}} - \left(\dot\theta + cs\left\{\frac{1}{T_{1x}} - \frac{1}{T_{1z}}\right\}\right)\langle I_Z\rangle + \gamma\frac{B_1}{s}\langle I_Y\rangle - \left\{\frac{c^2}{T_{1x}} + \frac{s^2}{T_{1z}}\right\}\langle I_X\rangle - \frac{3c^2-1}{2}\frac{\mathrm{i}}{\hbar}\langle[\mathcal{H}_{\mathrm{D}Z}, I_X]\rangle \tag{B.2b}$$

$$\frac{\partial\langle I_Y\rangle}{\partial t} = -\gamma\frac{B_1}{s}\langle I_X\rangle - \frac{\langle I_Y\rangle}{T_{1y}} - \frac{3c^2-1}{2}\frac{\mathrm{i}}{\hbar}\langle[\mathcal{H}_{\mathrm{D}Z}, I_Y]\rangle, \tag{B.2c}$$

with $s = \sin\theta$ and $c = \cos\theta$. $\mathcal{H}_{\mathrm{D}Z}$ is the doubly truncated part of the dipolar Hamiltonian that commutes with I_Z. The term $\dot\theta/\gamma\mathbf{j}$ is the inertia field due to the transformation to a time-dependent reference axis. In the adiabatic regime, defined by $\alpha = \dot\theta/(\gamma\ B_{\mathrm{e}}) \ll 1$, it can be shown that $\langle I_X\rangle = \langle I_Y\rangle = 0$ and the first two terms of equation (B.2a) are the expression of the spin-lattice relaxation in the rotating frame for strong r.f. fields [1,41]. This appendix seeks to evaluate the term proportional to $\langle I_X\rangle$ in equation (B.2a) that represents the decrease of $\langle I_Z\rangle$ due to the lack of adiabaticity. The equations of motion are expressed in terms of the raising and lowering operators $\langle I^+\rangle = \langle I_X\rangle + \mathrm{i}\langle I_Y\rangle$ and $\langle I^-\rangle$ its complex conjugate. We suppose that $\gamma B_{\mathrm{e}} \ll 1/\tau_0$, the reorientation correlation rate, for our compound which leads to T_{1x} independent of θ and $T_{1y} \approx T_{1x}$. First the adiabatic regime, $\alpha_{\max} < 0.1$, is examined where spin-spin interactions can be neglected. The influence of these processes will be discussed later on. As a consequence, one has

$$\frac{\partial\langle I^+\rangle}{\partial t} \approx -\mathrm{i}\gamma\frac{B_1}{s}\langle I^+\rangle - \frac{\langle I^+\rangle}{T_1^+} - \left(\dot\theta + cs\left\{\frac{1}{T_{1x}} - \frac{1}{T_{1z}}\right\}\right)\langle I_Z\rangle - s\frac{\langle I_0\rangle}{T_{1z}}, \tag{B.3}$$

with $1/T_1^+ = (1/T_{1y} + c^2/T_{1x} + s^2/T_{1z})/2$. Furthermore, the period of the cyclic passage is much smaller than the spin-lattice relaxation times. Hence, both $1/T_{1z}$ and $1/T_{1x}$ are negligible compared to $\dot\theta$:

$$\frac{\partial\langle I^+\rangle}{\partial t} \approx -\mathrm{i}\gamma\frac{B_1}{\sin\theta}\langle I^+\rangle - \frac{\langle I^+\rangle}{T_1^+} - \dot\theta\langle I_Z\rangle - \sin\theta\frac{\langle I_0\rangle}{T_{1z}}, \tag{B.4}$$

which, upon integration, gives the result:

$$\langle I^+\rangle = -\int_0^t \left\{\dot\theta(t')\langle I_Z\rangle + \sin\theta(t')\frac{\langle I_0\rangle}{T_{1z}}\right\} \times \exp\left\{-\int_{t'}^t \frac{1}{T_1^+} + \mathrm{i}\frac{\gamma B_1}{\sin\theta(t'')}\mathrm{d}t''\right\}\mathrm{d}t', \tag{B.5}$$

assuming that $\langle I^+\rangle = 0$ at a time $t = 0$. The expression for $\langle I^-\rangle$ is the complex conjugate of the above expression. For values of $t < T_1$, it is a good approximation to neglect $\langle I_0\rangle/T_{1z}$ compared to $\dot\theta\langle I_Z\rangle$ in the first bracket. Since the decay of $\langle I_Z\rangle$ is slow, it is replaced by a constant. Finally, the time variation of the longitudinal magnetization is given by:

$$\frac{\partial\langle I_Z\rangle}{\partial t} \approx -\langle I_Z\rangle\dot\theta(t)\int_0^t \dot\theta(t')\exp\left(-\int_{t'}^t \frac{1}{T_1^+}\mathrm{d}t''\right) \times\cos\left(\int_{t'}^t \frac{\gamma B_1}{\sin\theta(t'')}\mathrm{d}t''\right)\mathrm{d}t' - \langle I_Z\rangle\left(\frac{\cos^2\theta(t)}{T_{1z}} + \frac{\sin^2\theta(t)}{T_{1x}}\right) + \langle I_0\rangle\frac{\cos\theta(t)}{T_{1z}}, \tag{B.6}$$

which has been used in equation (6) in the text. Although the general form of our final expression contains a T_1^+-term in the first integral, the decrease of the magnetization due to the lack of adiabaticity of the fast passages is unrelated to spin-lattice relaxation mechanisms. This is best seen in the free spin limit ($T_1 \to \infty$), where our above equation (B.6) reduces to the integral form of the ordinary differential equation $\partial\langle\mathbf{I}\rangle/\partial t = \gamma\langle\mathbf{I}\rangle \times \mathbf{B}_{\mathrm{e}}$, an equation of motion that preserves the norm of the magnetization. In this limit, the first integral (the only non-vanishing term)

expresses the decrease of the projection $\langle I_Z \rangle$ due to a mistracking of the magnetization vector from the effective field direction. After several passages, the magnetization eventually reaches a steady state movement: a precession in a cone of summit angle of order α (the non-adiabaticity parameter) around the direction $\mathbf{B}_e + \dot{\theta}/\gamma\,\mathbf{j}$. For free spins, it implies that non-adiabatic effects alone cannot account for a substantial decrease of $\langle I_Z \rangle$ on a time scale of several passages. In condensed matter, however, the magnetization component perpendicular to the effective field direction quickly defocuses (thereby reducing the norm) principally because of spin-spin interactions.

The influence of these interactions are best seen in another rotating frame $\{X', Y', Z'\}$ where the direction Z' is aligned along the instantaneous axis of precession of the magnetization. The new system of differential equations is obtained by applying the unitary transformation $\exp(-\mathrm{i}\alpha I_X)$ to the equation system (B.2). Here second order corrections are examined and a more detailed analysis should take care of the new inertia field $\dot{\alpha}$. In this triply rotating coordinate system, the relaxation mechanisms along the X' and Y' directions are dominated by local field effects, which have a characteristic time of order T_2. The impact of these decays becomes prominent in the quasi-adiabatic regime ($\alpha_{\max} > 0.1$) when a significant percentage of the bulk magnetization is projected perpendicular to the precession axis. A complete analytical account of these effects is complicated because the local field in the triply rotating frame oscillates with time. We have simplified the problem by adding a relaxation term $-\langle I_q \rangle / T_2$ to the equation of motion of the $q = X', Y'$ component respectively. This is equivalent to approximating these interactions to a time independent local field with a Lorentzian lineshape. Taking $T_2 = 40$ μs and solving numerically the linear differential equations, we find that, when $\alpha_{\max} > 0.1$, the percentage of bulk magnetization, which vanishes after *one* passage because of spin-spin interactions, corresponds roughly to the change in $\langle I_{Z'} \rangle$ produced by the lack of adiabaticity, of order $1 - \cos(\alpha_{\max}/2)$.

References

1. A. Abragam, *Principles of Nuclear Magnetism* (Oxford University Press, 1961).
2. J.A. Sidles, Appl. Phys. Lett. **58**, 2854 (1991).
3. J.A. Sidles, Phys. Rev. Lett. **68**, 1124 (1992).
4. J.A. Sidles, D. Rugar, Phys. Rev. Lett. **70**, 3506 (1993).
5. J.A. Sidles, J.L. Garbini, K.J. Bruland, D. Rugar, O. Züger, S. Hoen, C.S. Yannoni, Rev. Mod. Phys. **67**, 249 (1995).
6. D. Rugar, C.S. Yannoni, J.A. Sidles, Nature **360**, 563 (1992).
7. D. Rugar, O. Züger, S. Hoen, C.S. Yannoni, H.M. Vieth, R.D. Kendrick, Science **264**, 1560 (1994).
8. Z. Zhang, P.C. Hammel, P.E. Wigen, Appl. Phys. Lett. **68**, 2005 (1996).
9. O. Züger, D. Rugar, Appl. Phys. Lett. **63**, 2496 (1993).
10. P.C. Hammel, Z. Zhang, G.J. Moore, M.L. Roukes, J. Low Temp. Phys. **101**, 59 (1995).
11. O. Züger, S.T. Hoen, C.S. Yannoni, D. Rugar, J. Appl. Phys. **79**, 1881 (1996).
12. A. Schaff, W.S. Veeman, Appl. Phys. Lett. **70**, 2598 (1997).
13. B.J. Suh, P.C. Hammel, Z. Zhang, M.M. Midzor *et al.*, J. Vac. Sci. Technol. B **16**, 2275 (1998).
14. C. Ascoli, P. Baschieri, C. Frediani, L. Lenci, M. Martinelli, G. Alzetta, R.M. Celli, L. Pardi, Appl. Phys. Lett. **69**, 3920 (1996).
15. K. Wago, O. Züger, R. Kendrick, C.S. Yannoni, D. Rugar, J. Vac. Sci. Technol. B **14**, 1197 (1996).
16. K. Wago, O. Züger, J. Weneger, R. Kendrick, C.S. Yannoni, D. Rugar, Rev. Sci. Instrum. **68**, 1823 (1997).
17. K. Wago, D. Botkin, C.S. Yannoni, D. Rugar, Phys. Rev. B **57**, 1108 (1998).
18. K. Wago, D. Botkin, C.S. Yannoni, D. Rugar, Appl. Phys. Lett. **72**, 2757 (1998).
19. K.J. Bruland, W.M. Dougherty, J.L. Garbini, J.A. Sidles, S.H. Chao, J. Appl. Phys. **73**, 3159 (1998).
20. A. Schaff, W.S. Veeman, J. Magn. Res. **126**, 200 (1997).
21. R. Verhagen, C.W. Hilbers, A.P.M. Kentgens, L. Lenci, R. Groeneveld, A. Wittli, H. van Kempen, Phys. Chem. Chem. Phys. **1**, 4025 (1999).
22. S.R. Miller, R. Blinc, M. Brenman, J.S. Waugh, Phys. Rev. **126**, 528 (1962).
23. D.E. O'Reilly, T. Tsang, J. Chem. Phys. **46**, 1291 (1967).
24. S. Guillous, O. Klein (to be published).
25. Near the symmetry axis, $\nabla B_{\mathrm{cyl}} \approx (\partial B_{\mathrm{cyl}}/\partial z)\mathbf{k}$.
26. 99.999% purity (Aldrich).
27. The value is measured in a 1 T field using a coil detection (A. Dooglav). In this experiment, the powder is made of coarse grains.
28. R.E. Richards, T. Scaefer, Trans. Faraday Soc. **57**, 210 (1961).
29. The sample mass and shape are stable for the duration of the experiment.
30. Using the static flexion of the cantilever as a temperature sensor, we estimate to +1.5 °C the elevation of the sample temperature during the r.f.-irradiation.
31. We can do this approximation because all slices are phase coherent.
32. The width of the probed slice is proportional to $\sqrt{1.2(\Omega/\gamma)^2 + B_1^2}/g$.
33. The fast relaxation $T_{1\mathrm{s}}$ can also partially explain the positive offset b.
34. In the limit $B_1 > g\times$thickness, τ^{-1} equals to $(1/T_1 + 1/T_2)/2$ [1].
35. E. Fukushima, S.B.W. Roeder, *Experimental pulse NMR* (Addison-Wesley, 1981)
36. E.O. Schlemper, W.C. Hamilton, J. Chem. Phys. **44**, 4498 (1966).
37. J.L. Hutter, J. Bechhoefer, Rev. Sci. Instrum. **64**, 1868 (1993).
38. Comments about MRFM noise can be found in `http://weber.u.washington.edu/~sidles/`.
39. The phase noise of our setup is estimated from fast adiabatic passage measurements on de-ionized H_2O in a 1 T field with a coil detection and comparing the apparent τ_{m} obtained with the VCO and a Marconi 2023 synthesizer.
40. M. Goldman, *Spin temperature and Nuclear Magnetic Resonance in solids* (Oxford University Press, 1970).
41. C.P. Slichter, *Principles of Magnetic Resonance*, 3rd edn. (Springer, Berlin, Heidelberg, New York, 1996).